



Full length article



Influence of group IV element on basic mechanical properties of BCC medium-entropy alloys using machine-learning potentials

Ivan Lobzenko ^{a,*}, Yoshinori Shiihara ^b, Hideki Mori ^c, Tomohito Tsuru ^{a,d,e,**}^a Nuclear Science and Engineering Center, Japan Atomic Energy Agency, 2-4 Shirakata, Tokai-mura, 319-1195, Ibaraki, Japan^b Graduate School of Engineering, Toyota Technological Institute, 2-12-1 Hisakata, Tempaku-ku, Nagoya, 468-8511, Aichi, Japan^c Department of Mechanical Engineering, College of Industrial Technology, 1-27-1 Nishikyo, Amagasaki, 661-0047, Hyogo, Japan^d Elements Strategy Initiative for Structural Materials (ESISM), Kyoto University, Yoshida, Honmachi, Sakyo-ku, Kyoto, 606-8501, Japan^e PRESTO, Japan Science and Technology Agency, 4-1-8 Honcho, Kawaguchi, 332-0012, Saitama, Japan

ARTICLE INFO

ABSTRACT

Keywords:

High-entropy alloys
Machine-learning potentials
Elastic constants

In order to elucidate the origin of excellent mechanical properties of high-entropy alloys (HEA), it is essential to develop the atomic-level depiction of defect structures, taking into account the influence of composition. Especially in body-centered cubic (BCC) HEA an alteration of constituent elements may lead to a dramatic change in the behavior on the macroscopic level. To study that effect, we employed a machine learning technique and constructed highly accurate robust potentials for two BCC medium-entropy alloys: MoNbTa and ZrNbTa. Even though they have close composition, the mechanical properties of the two alloys differ not only quantitatively, but also qualitatively. We show that the group IV element Zr decreases values of bulk and elastic constants. The influence of short-range order on stacking fault and twin boundary energies is discussed. Also, we show the difference in the screw dislocation core shapes between the two alloys. The cores of $\langle 111 \rangle$ screw dislocations in the ZrNbTa case demonstrate a non-compact shape substantially extended on the $\langle 110 \rangle$ plane.

1. Introduction

The last twenty years showed constant growth in scientific attention towards materials formed by multiple (more than four) principal constituent metallic species (referred to as high-entropy alloys (HEAs) [1]). HEAs exhibit outstanding mechanical properties, such as the coexistence of high strength and ductility [2]. Due to nearly infinite compositional space, such materials provide new opportunities for industry, but at the same time pose increased difficulty for systematic studies.

Historically, the works on face-centered cubic (fcc) FeCrMnNiCo alloy [3–5] (so-called Cantor alloy) drew now constantly growing interest to HEA. Recently it was also shown that unique mechanical properties can be achieved in CrCoNi medium-entropy alloy (MEA) at cryogenic temperatures [6]. Theoretical studies on fcc HEAs demonstrate the potential to control mechanical properties by doping using metalloids [7,8]. Another type of HEAs having a body-centered cubic (BCC) structure also exhibits remarkable mechanical strength [9,10]. These alloys withstand elevated temperatures and are therefore called refractory HEA.

Theories for mechanisms behind the properties of BCC HEAs are now in active development. Here, as in alloys of other types, mobility of screw dislocations plays an important role in solid solution strengthening [11–13]. However, special attention is given to complex effects, such as jogs (or cross-kinks) formation, appearing during the motion of screw dislocations. Also, unlike pure (and dilute) BCC metals, in BCC HEAs motion of edge dislocations have a recognizable influence on strength, especially when high temperatures are taken into account [14]. Extraordinary ductility in HEAs is attributed to the process of dislocations emission from the tip of the sharp crack, which appears more favorable compared to the brittle cleavage induced by the crack [15].

Computational studies provide viable tools to investigate the role of each basic characteristic of HEAs. Due to high computational cost, the need of using rather big special quasi-random structures (SQS) complicates the application of the first-principle density-functional (DFT) approach [16]. Classical molecular dynamics (MD) is spared this problem but is suffering from the lack of appropriate interatomic potentials with sufficient accuracy. Though EAM-type potentials [17,18] are actively used for testing theories of mechanical properties of HEAs, it was

* Corresponding author.

** Corresponding author at: Nuclear Science and Engineering Center, Japan Atomic Energy Agency, 2-4 Shirakata, Tokai-mura, 319-1195, Ibaraki, Japan.

E-mail addresses: lobzenko.ivan@jaea.go.jp (I. Lobzenko), tsuru.tomohito@jaea.go.jp (T. Tsuru).

shown previously that EAM potentials may fail in reproducing features of dislocations in BCC metals and alloys [15,19]. Mostly, classical interatomic potentials are tailored to represent one principal element. In HEAs, neither element can be referred to as the main one, which makes usual potentials fail to reproduce intrinsically heterogeneous characteristics such as short-range order. That is why a new technique of building potentials for MD should be applied, which is based on machine learning [20]. It allows the development of interatomic potentials (machine-learning potentials or MLP) with high accuracy for virtually any system [21,22].

Works on BCC high entropy alloys show that some systems are brittle. Quinary MoNbTaVW and quaternary MoNbTaW demonstrate such behavior. However, if some atomic species are substituted with group IV elements, the material drastically changes its behavior, becoming ductile [23,24]. TaNbHfZrTi alloy (so-called Senkov alloy) is one of the representatives of BCC-HEA having excellent ductility [23]. Molecular dynamics simulations may help to clarify the origins of that properties change, but the question of potentials must be addressed.

Using MLP built on DFT data, the phase stability of NbMoTaW was studied [25]. Another MLP density of neighbors as descriptors was developed for that refractory HEA to examine the formation of the short-range order [26]. To study mechanical properties, a robust interatomic potential is needed, which would be capable of reproducing potential energy surface in the regions corresponding to defects, such as grain boundaries and dislocations. Also, to the best of our knowledge, there are no MLPs available for systems with group IV elements.

This work is devoted to building the potentials for two medium-entropy alloys: MoNbTa and ZrNbTa. We aim at developing potentials that will reproduce qualitative and quantitative differences between two close materials. These alloys were chosen due to the possibility to unveil the role of group IV element Zr in the mechanical properties of MEAs.

2. Methods

The training data (data set) was generated in density-functional calculations using the VASP package [27–29]. Structures varied in size from single elementary cells for basic structures to small SQS (having $3 \times 3 \times 3$ BCC conventional cells, 54 atoms) and big SQS (having $6 \times 6 \times 6$ BCC cells, 432 atoms) systems. More details about the data set will be discussed below, while here we give technical parameters of the calculations. The plane-wave cut-off energy was set to 300 eV, and Fermi smearing of 0.01 eV was used to facilitate calculations. The data set consists of structures of different sizes and it is important to keep k -points density uniform, otherwise, total energies correspondent to structures with different k -points densities will be incomparable. In the present study, we set our k -points spacing in the Monkhorst-Pack grid to 0.01 \AA^{-1} . The self-consistent loops were deemed converged after reaching the 10^{-5} eV difference in energy. We used the projector augmented wave method implemented in VASP with the Perdew–Burke–Ernzerhof GGA exchange–correlation functionals [30].

Machine learning is an umbrella term and its interatomic potentials are built on a variety of basic schemes, among which two are the most common: Gaussian kernel regression [31,32], and artificial neural networks [33]. In the latter case, which is used in the present work, there are (usually two) hidden layers of functions between the input and output data. The input layer is the one responsible for the representation of the system and therefore consists of descriptor functions. Descriptors are widely chosen in the form of symmetrical functions correspondent to pair-wise (radial functions) and triple (angular functions) [20] interactions, or in a peculiar form of higher-order functions operating on atomic neighbors density [34]. We employed Chebyshev polynomials as the descriptors, which have proven to be more efficient in the case of systems with many species [35]. We used

ænet package [36,37] for training the potentials. Hyperbolic tangent worked as an activation function for the hidden layers.

The neural network works for each atom in the system: the input layer, as it has been said, receives the coordinates of the atom's neighbors, and the output is only one property — atomic energy. The total energy of one structure is the sum of the resulting energies of all atoms. That approach allows variations in the total number of atoms, while the number of descriptors for each atom is fixed [38]. Originally only the total energies of structures were to be used for training the network. Though it decreases the accuracy in representations of atomic forces, there is an important qualitative advantage of such an approach. By keeping the analytical connection between energies and forces, the framework sharply limits the area where systems are represented phenomenologically. When energies are fitted, many other important physical quantities (such as pair forces and atomic stresses) can be calculated analytically [39].

To assess the quality of potentials, we discuss several basic properties of MoNbTa and ZrNbTa. One of the main characteristics of multi-component alloys is mean-square atomic displacement [40], which can be calculated as an averaged squared atomic displacement from the ideal lattice points:

$$\langle u_{\text{atomic}}^2 \rangle = \frac{\sum_i |\mathbf{r}_i - \mathbf{r}_{\text{ideal}}|^2}{N}, \quad (1)$$

where \mathbf{r}_i denotes the coordinate vector of atom i in the relaxed configuration, while $\mathbf{r}_{\text{ideal}}$ is the coordinate vector of the correspondent ideal lattice point, and N is the total number of atoms. MSAD can be observed in real experiments [41] and plays an important role in sluggish diffusion, one of the distinguishing features of HEA. We also take into consideration bulk and elastic constants, stacking fault (SF), and twin energy.

Calculations in classical approximation were carried out using Large-scale Atomic/Molecular Massively Parallel Simulator (LAMMPS) [42,43] with the library for ænet developed by a co-author of this study H. Mori [44,45]

3. Data set

The content of a data set is one of the main factors affecting the quality of a potential to be built. Its importance increases in the case of machine-learning potentials based on artificial neural networks because no physics is included in the energy function's mathematical structure (the neural network itself). The only exception is the geometrical symmetry of descriptors, which avoids the non-necessary listing of symmetrically equivalent arrangements of atoms in a data set. So far, the only rule for building a data set is to include as many different atomic arrangements as possible; that is why atoms are given random distortions to cover potential energy surface (PES).

The data set structure is shown in Table 1. The main part consists of structures with short-range order (SRO). At first, random SQS models were obtained using the alloy theoretic automated toolkit (ATAT) [46]. Then, Monte Carlo (MC) calculations were used to explore if SRO can develop in the studied alloys. A Canonical (NVT) ensemble was chosen with the temperature of 100 K. The SRO formation in DFT calculations is not the subject of study in the present paper, so we have chosen low temperature to ensure major influence from atomic arrangements. After 2000 MC steps done by DFT with low k -points density ($3 \times 3 \times 3$ k -points grid was used for 54-atoms structure and only the Γ -point - for 432-atoms structure) and without optimization of atomic positions, some structures were chosen for relaxation and better k -density calculations to be added to the data set. It is important that not only structures accepted during MC were chosen, but also those whose energies are higher, so that PES was covered in those regions, too. All structures in the data set went through both lattice vectors' transformations and atomic positions' distortions. We applied transformations and distortions up to 10% of the lattice parameter to ensure the robustness of potentials.

Table 1

Structure of the data sets used for training MLPs for MoNbTa and ZrNbTa alloys. (X) stands for Mo or Zr atomic species. The magnitudes of lattice vectors' transformation and positions' distortions are expressed in percentages of the cell parameter a . Basic structures were at first equilibrated in the shape of one conventional cell, then multiplied by 2 in all directions for atomic positions distortions. SRO was captured in small (54 atoms) and big (432 atoms) SQS structures. Structures for stacking fault had six layers in the (110) direction (total 180 atoms), while structures with twins had 24 atomic layers in the (121) direction (total 360 atoms). Test data was taken as 5% of all structures scattered randomly across the data set.

| Atomic species | Lattice | Lattice vectors' transformation magnitude | Positions' distortion magnitude | N data set entries |
|--------------------|--------------------------------------|---|---------------------------------|--------------------|
| (X) Nb Ta | BCC, FCC, HCP, diamond, simple cubic | [−5,0,+5]% | 5% | 600 |
| | | | | |
| (X)NbTa →single | BCC | [−3,+3]% | 5% | 1620 |
| (X)NbTa | BCC with SRO | [−5,−3,0,+3,+5] % | [5,10]% | 10780 |
| (X)NbTa | BCC 110 slip system | [−5,+5]% | 5% | 2000 |
| (X)NbTa | BCC with(112) twin boundary | [−5,+5]% | 5% | 2000 |
| | | | Total | 18200 |

Visualization of data has general importance for the control of potential quality, for a long time is required before any properties of modeled materials can be seen. The number of descriptors to represent the geometry of systems is usually too big for any kind of visualization. That is why it is difficult to assess the quality of the database preliminary to the training process. However, the principal component analysis (PCA) [47] may be applied to decrease the dimensionality of the problem and plot the entries of the data set. Even though it is not a rigorous study tool, it can give a better understanding of the task at hand.

We show here with PCA that a small SQS model would not be enough for a robust potential. In Fig. 1, the analysis is done for one small (54 atoms) and one big (432 atoms) SQS structure. It also shows data set entries from initial random structures and from structures with SRO gained in MC calculations. It can be seen that, as expected, entries from big SQS cover bigger space. That is why even though big SQS structures need a large amount of resources, they must be present in the data set. It is worth mentioning that structures with lower SRO (marked “init” in Fig. 1) produce higher variability of descriptors.

4. Results

4.1. Training of ANN potential

The process was performed until the mean average error in structures energies was lower than 10^{-3} [eV]. In Fig. 2 the comparison of DFT data (energies and forces) and ANN data is shown. Both test and train energies locate near the diagonal line ($y = x$) showing that energy predicted by ANN potentials is consistent with the DFT data set. The objective function does not include forces, which is why points dispersion is larger (see the insets in Fig. 2(a) and (b)), however, it is clear that no systematical error emerged.

4.2. Short-range order

To introduce SRO to a random structure, we conducted MC simulations with the Metropolis–Hastings algorithm and calculated total SRO, where the ordering parameter for each atomic pair is a slightly modified Warren–Cowley parameter [48]:

$$\delta_{ij} = n \left(p_{ij} - p_{ij}^{\text{random}} \right), \quad (2)$$

where n is the number of neighbors taken into account, p_{ij}^{random} is the frequency of ij pair in the perfectly random alloy, and p_{ij} is calculated

the frequency of that pair in the actual structure. A value close to zero means randomness, while positive (negative) values correspond to an increase (decrease) in the frequency of pairs of a given type. This makes the parameter easy to analyze on diagrams for many component materials. Total SRO for the structure is calculated as summarized absolute values of all δ_{ij} parameters. The comparison of MC simulations using ANN potential and DFT (see Fig. 3) shows that the potential is reproducing the emergence of the SRO. We have confirmed similarities in energy differences and SRO patterns for small systems without atomic positions relaxations (due to the fact that in DFT the optimization needs much time). Further studies of SRO by means of classical modeling with MLP were done for a larger number of MC steps (4000 instead of 2000 in DFT) and including optimization of atomic positions at each MC step. Our potentials allow this because of the fact that some structures from first-principles MC have been put through relaxation and added to the data set.

Using new potentials for both alloys, MC simulations were carried out for three temperatures: 100, 300, and 800 K. It is worth noting that classical MD allows much wider statistics compare to DFT calculations, where only one temperature value of 100 K was used. Also, it is only with new potentials we can perform MC with relaxation at each step, which is important in the ZrNbTa case because of the more considerable effect of relaxation on total energy. As expected, the total value of SRO after the same number of MC steps decreases with an increase in temperature. Results for MoNbTa (see Fig. 4(a,b,c)) show that the Mo-Ta pair is attractive, while the Ta-Ta pair is repulsive. On the contrary, in ZrNbTa, as can be seen in Fig. 4(d,e,f), the number of Ta-Ta pairs grows with MC steps. It is the Zr-Ta pair, that demonstrates repulsion. It is expected that these two alloys show the different influences of SRO on mechanical parameters.

4.3. MoNbTa and ZrNbTa basic material properties

For structures in the data sets and those that were not included, the MSAD was calculated using VASP and new potentials. In total nine structures were used: one small $3 \times 3 \times 3$ BCC conventional cells (54 atoms) and one big $6 \times 6 \times 6$ cells (432 atoms), both of which were included in the data set, and six other structures of the medium size, which had $5 \times 5 \times 5$ cells (250 atoms), out of which only one was in the data set. That again ensures more reliable statistics compare to the VASP calculations.

We present the root square of MSAD in Fig. 5(a) and (c) due to easier interpretation of this parameter as lattice distortions in Å units. As can be seen, both potentials for MoNbTa and ZrNbTa overestimate

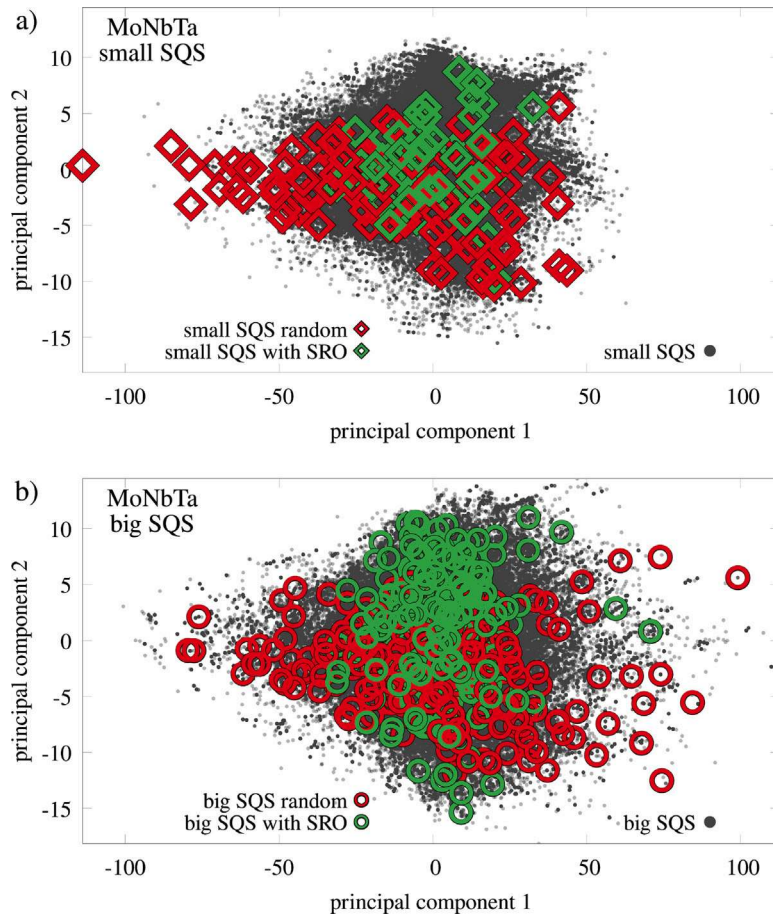


Fig. 1. PCA example: (a) small SQS structures with 54 atoms, (b) big SQS structures with 432 atoms. Among both big and small structures two particular atomic arrangements are highlighted: one small SQS structure before (after) MC calculations correspond to empty light red (green) diamonds; one big SQS before (after) MC calculations correspond to empty light red (green) circles.

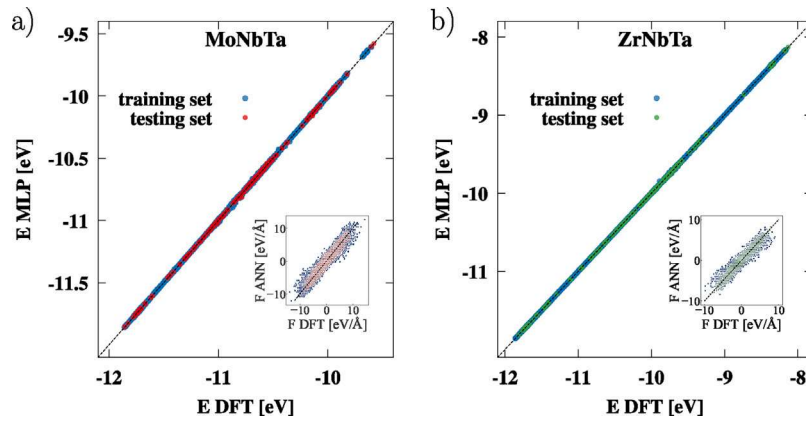


Fig. 2. Comparison of energies (main plots) and forces (insets) of MLP and DFT for (a) MoNbTa and (b) ZrNbTa.

the MSAD if compared to DFT results. Nevertheless, a clear difference between the two alloys is seen: ZrNbTa alloy demonstrates much higher atomic positions' distortions. Also, differences between the two materials are established in values of bulk modulus and elastic constants (see Fig. 5(b) and (d)). The bulk modulus of MoNbTa is higher than the one of ZrNbTa, and so are all calculated elastic constants. It is worth mentioning that for the training of the potentials some parts of the data set were proven to be more important than others (details can be found in supplementary material). In particular, only if structures with defects (SF and twin boundaries) were included in the data set, did

the values of bulk and elastic constants predicted by ANN potentials become consistent with the DFT results.

Elastic constants of an alloy are known to be dependent on the number of valence electrons [49]. Our results also show a decrease in elastic constants when Mo (group VI element) is substituted with Zr (group IV element). Overall elastic constants of ZrNbTa are not only lower but also demonstrate close values of C_{11} and C_{12} .

To calculate SF energy, structures were prepared and oriented so that the z-axis is aligned with BCC [110] direction (see Fig. 6(a)). The structure has six layers in [110] direction, three of which are

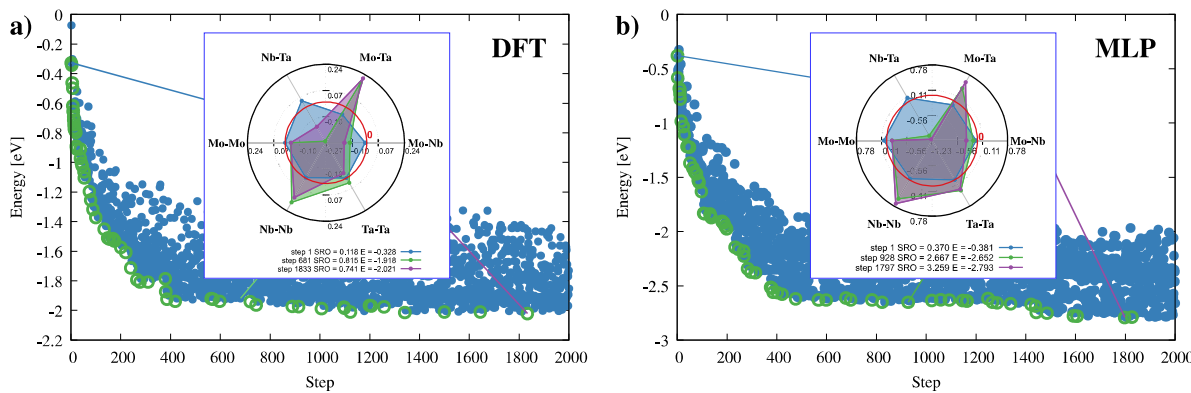


Fig. 3. Monte Carlo simulations using (a) DFT and (b) MLP. A small SQS structure with 54 atoms without relaxation of atomic positions was used.

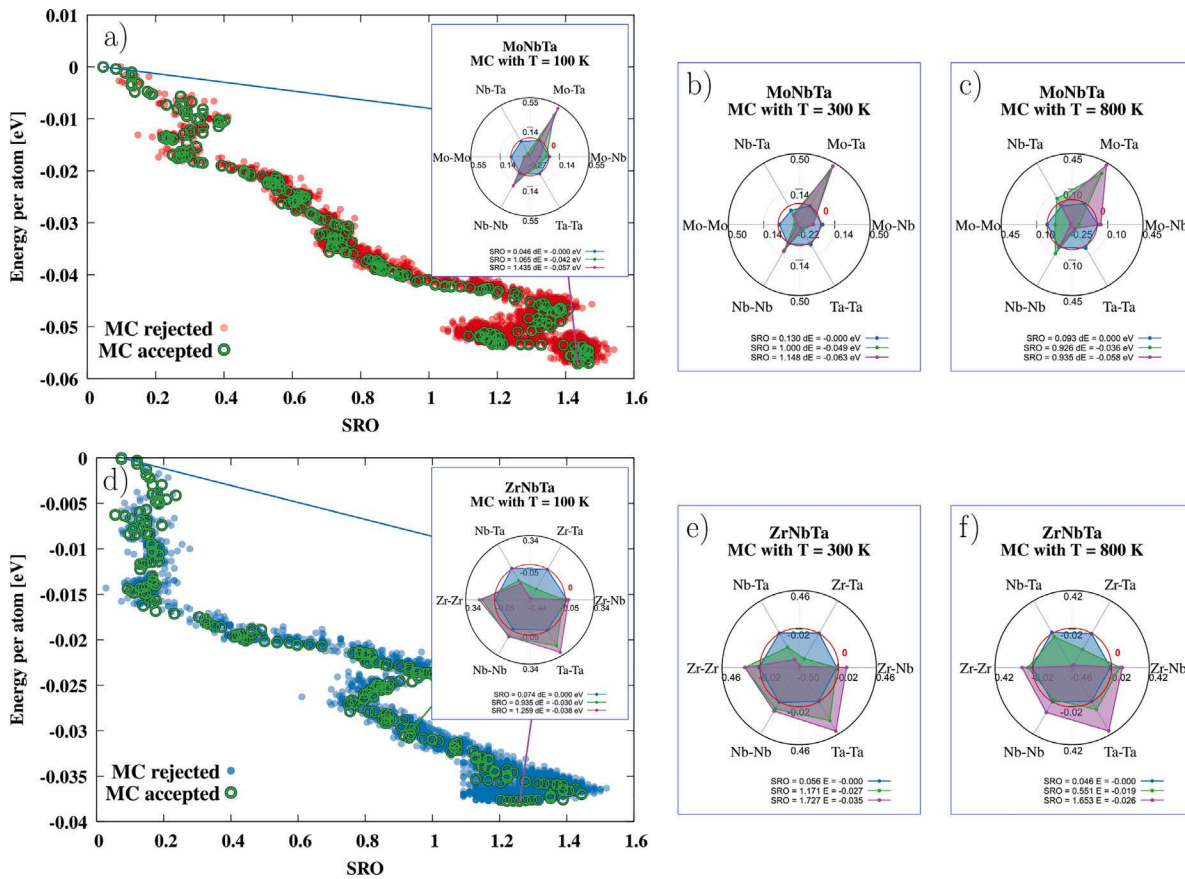


Fig. 4. SRO formation in two BCC-MEA. (a) Per atom energy change on SRO through MC simulations at 100 K, (b) 300 K, and (c) 800 K in MoNbTa. (d)–(f) Same as (a)–(c) but in ZrNbTa. The big SQS structure (with 432 atoms) is used and atomic relaxation is performed at every MC step.

displaced to introduce the SF as shown in Fig. 6(b). The calculation cell as a whole is also transformed accordingly to keep *only one* SF using periodic boundaries. Due to the random distribution of atomic species, the SF inserted between different layers yields slightly different energies, so averaging of all possible SF positions should be done. The maps of averaged generalized SF are shown in Fig. 6 for both MoNbTa and ZrNbTa. Results of stacking fault calculations show consistency between ANN and DFT results.

Structures used for modeling the SF (and twin boundary, as discussed later) were also put through the MC scheme to analyze SRO influence on the SF energy. We compare in Fig. 6(e,f) values of SF energy in BCC [111] direction with the interface normal being (110). It appears that in MoNbTa SRO increases SF energy only slightly. However, SF energy in ZrNbTa shows almost no changes with varying

SRO. It should be noted that DFT results show no change in SF energy of MoNbTa with SRO at 300 K temperature, which is different from the trend in MLP calculations. But that is attributed to the fact that only one structure was used in DFT calculations, while the results of three different structures are averaged in the MLP case.

To calculate twin boundary energy, the structure with (112) twin was used (as shown in Fig. 7(a)). The value of the twin boundary energy was calculated as the difference between energies of the structure with and without the twin boundary, divided by the doubled interface area, S : $\gamma_{\text{twin}} = (E_{\text{twin}} - E_0) / (2S)$. Doubling of the interface area is needed due to the presence of two twin boundaries in the structure. Results, presented in Fig. 7(b,c) for random alloys and after MC again show a clear difference between the two alloys. In the case of MoNbTa, the energy is much higher and growing when SRO is introduced. ZrNbTa

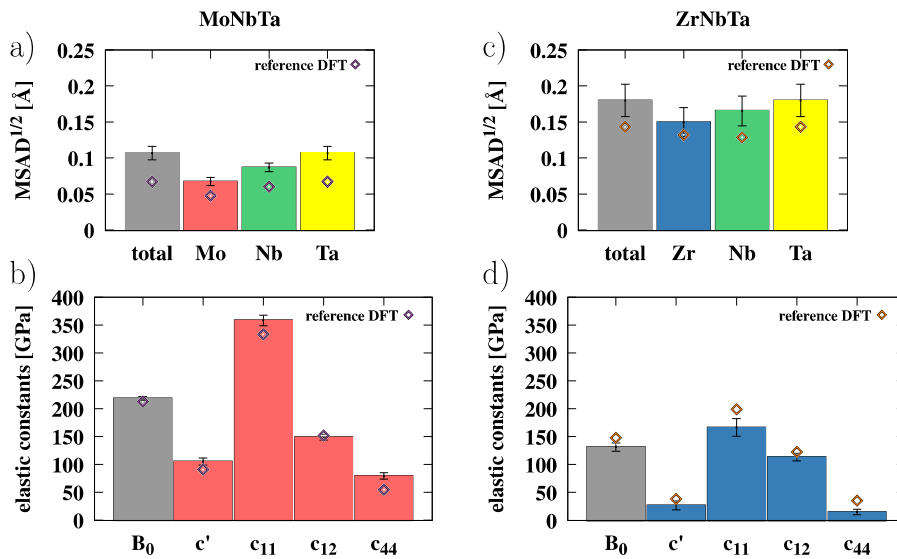


Fig. 5. Fundamental materials properties in two BCC-MEA. (a) MSAD^{1/2} and (b) elastic constants in MoNbTa. (c) Same as (a) but in ZrNbTa. (d) Same as (b) but in ZrNbTa.

on the contrary shows low twin boundary energy and small indecisive change with SRO.

4.4. Screw dislocation core in MoNbTa and ZrNbTa

To study the shape of screw dislocation, we introduced it at the center of the (111) plane of the structure shown in Fig. 8(e). The length of the simulation cell along ⟨111⟩ direction was $10b$, where b is the Burgers vector. The total number of atoms was 43 200, which means that the formalism of SQS may be omitted. However, for the reliability of results for both alloys, we have prepared twenty such structures with different random distributions of atoms and performed statistical analysis on them. Screw dislocation cores in structures of this size can be treated only in classical MD. It allows better randomness as the SQS formalism is no longer needed. Also, the same dislocation can be analyzed across several layers, which is inaccessible in DFT simulations.

First, we fully optimized the structures without the dislocation, then all atoms were displaced in z direction according to the elastic solution for the displacement field of a screw dislocation [50]. Naturally, that implies that the displacement in z direction increases gradually with the angle in xy plane to give the discontinuity of one Burgers vector at the cut surface defined by $y = y_c$, $x > x_c$:

$$\Delta z_i = b \left[\frac{1}{2\pi} \arctan \left(\frac{y_i - y_c}{x_i - x_c} \right) + 0.5 \right], \quad (3)$$

where b is the Burgers vector, i is an atomic index, and (x_c, y_c) is the geometrical center of the dislocation core, which was chosen to summon a screw dislocation. We consider here only the screw dislocations with stable easy core configuration (see [19] for definitions of easy, hard, and split cores). Finally, optimization was done for all atoms except those located more than 60 Å from the center. We show in Fig. 8(a,b) the atomic configurations for the dislocations cores in the region spanned by one Burgers vector (see supplementary material for figures of all layers). Arrows correspond to the differential displacements (DD) of the pairs of atoms [51].

In previous works on MoNbTaW refractory HEA two types of screw dislocation cores were found. Due to the inhomogeneity of chemical environments, the core may suffer the extension on the (110) plane, which makes it non-compact if such an extension is large. It is seen from DFT modeling of the screw dipole system [52], that majority of cores are compact in MoNbTaW HEA similar to the core shape in pure BCC metals [53]. Other MLPs built for MoNbTaW also find both types of dislocation cores with the majority of the compact type [26,54],

though even for compact-type cores small extension in (110) plane can be observed. We analyze the core shape by calculating (and presenting in Fig. 8(c,d)) the distribution of the DD absolute values of three central atoms (highlighted in Fig. 8(a,b)) across all layers and structures. As can be seen, for both alloys maximum value of the DD distribution locates at 33% of the Burgers vector, as expected. However, the maximum in MoNbTa is more pronounced indicating the majority of cores to be only slightly extended on the (110) plane. We note that the equiatomic composition of MoNbTaW HEA has a smaller fraction of Nb and Ta. These species, as group V elements, exhibit decreased energy of the split-core configuration in contrast to Mo and W group VI elements [55]. That is why it is natural to expect the screw cores of MoNbTa to be less compact than that of MoNbTaW. From the comparison of screw core structures of MoNbTa and ZrNbTa, it is evident that the distribution of DD values in the latter has larger width clearly showing non-compact screw dislocation cores.

5. Discussion

We want to highlight the fact that the basic properties of the materials discussed in Section 4.3 were obtained using not only structures in the data set for potentials training. Specifically, only three out of nine SQS models were put into the data set. Therefore our new MLPs exhibit robustness: they are capable of reproducing consistent data even outside of the data set. That is possible due to the inclusion of a wide range of atomic positions' distortions and structures with different SRO. In addition, our calculations revealed that the type of constituent elements has a dominant effect on the fundamental properties rather than SRO formation in BCC-MEA/HEA. Group IV elements, in particular, are essential factors that can alter elastic constants and SF energy significantly. Trends in elastic constants and SF energies allow us to compare ZrNbTa alloy with so-called gum-metals [56], alloys that approach elastic instability. In this connection, as expected the shape of dislocations in MoNbTa and ZrNbTa are different: the majority of cores in ZrNbTa are non-compact.

Significantly lower unstable stacking energy along with a large screw dislocation core in ZrNbTa is strong evidence of ductility [15], however, the anisotropy should be taken into account. The simple Zener anisotropy factor ($A = 2c_{44}/(c_{11} - c_{12})$) gives values of 0.76 for MoNbTa and 1.81 for ZrNbTa, showing that the latter alloy possesses significant anisotropy. The influence of anisotropy is negative on ductility, so further examination should be carried out.

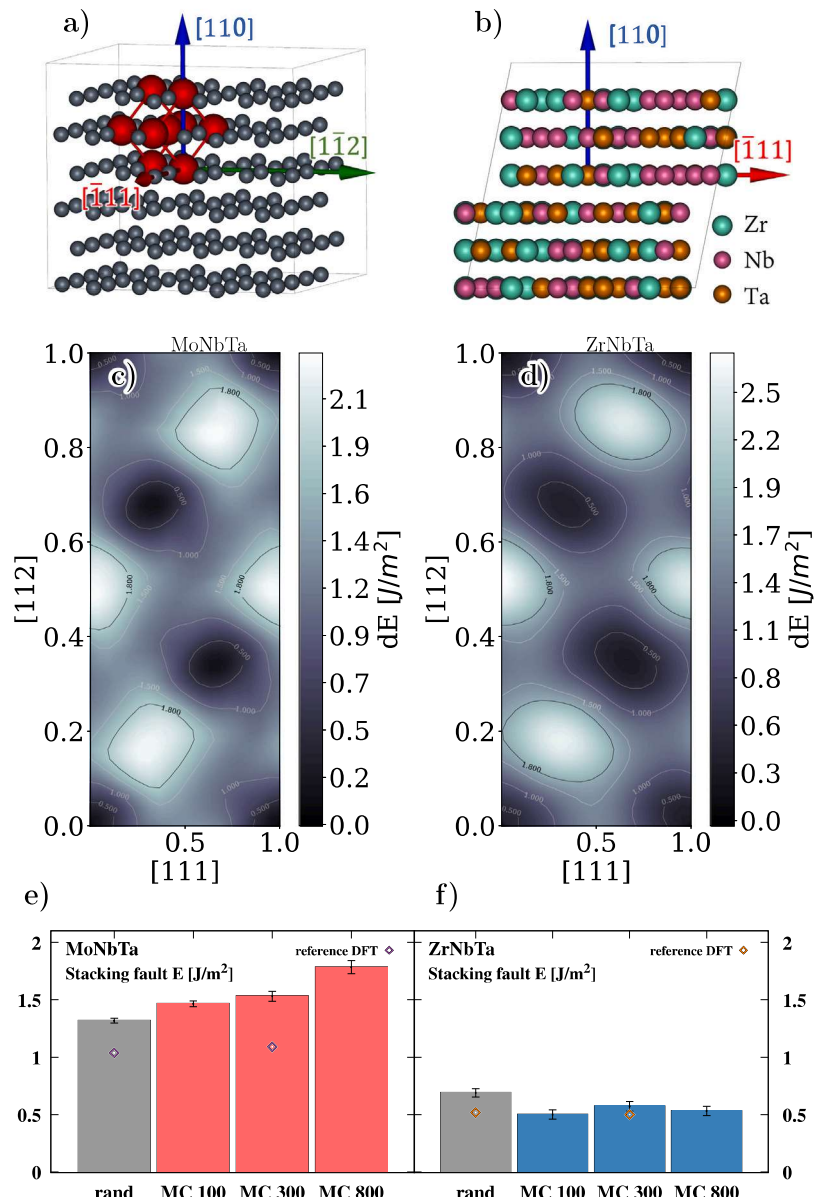


Fig. 6. (a) Initial structure (red atoms depict BCC unit cell) and (b) shifted upper half to introduce SF. 2D map of generalized SF energy in (c) MoNbTa and (d) ZrNbTa. Maximum SF energy of random and structures with SRO for shift in [111] direction for (e) MoNbTa and (f) ZrNbTa.

6. Conclusion

We built interatomic potentials based on neural networks for two medium-entropy BCC alloys: MoNbTa and ZrNbTa. New potentials can reproduce basic properties such as MSAD, elastic constants, stacking fault, and twin boundary energies. With results obtained using new potentials, it was shown that the substitution of group VI element Mo by group IV element Zr elastic constants of the material drastically changes, which drags the alloy closer to the elastic instability region. Current work opens the possibility for further studies of the mechanical properties of MoNbTa and ZrNbTa using classical molecular dynamics.

CRediT authorship contribution statement

Ivan Lobzenko: Calculations, Data analysis, Writing – original draft. **Yoshinori Shiihara:** Methodology, Validation. **Hideki Mori:** Conceptualization, Methodology, Data curation. **Tomohito Tsuru:** Conceptualization, Supervision, Writing – review & editing.

Declaration of competing interest

The authors declare that they have no known competing financial interests or personal relationships that could have appeared to influence the work reported in this paper.

Data availability

The data (interatomic potentials) is shared as supplementary materials.

Acknowledgments

This work was supported by JSPS KAKENHI, Japan (Grant Nos. 18H05453, 21K20418, 22H01762, 22H05041). TT acknowledges the support of JST PRESTO, Japan (Grant No. JPMJPR1998). Simulations were performed on the large-scale parallel computer system with SGI 8600 at JAEA.

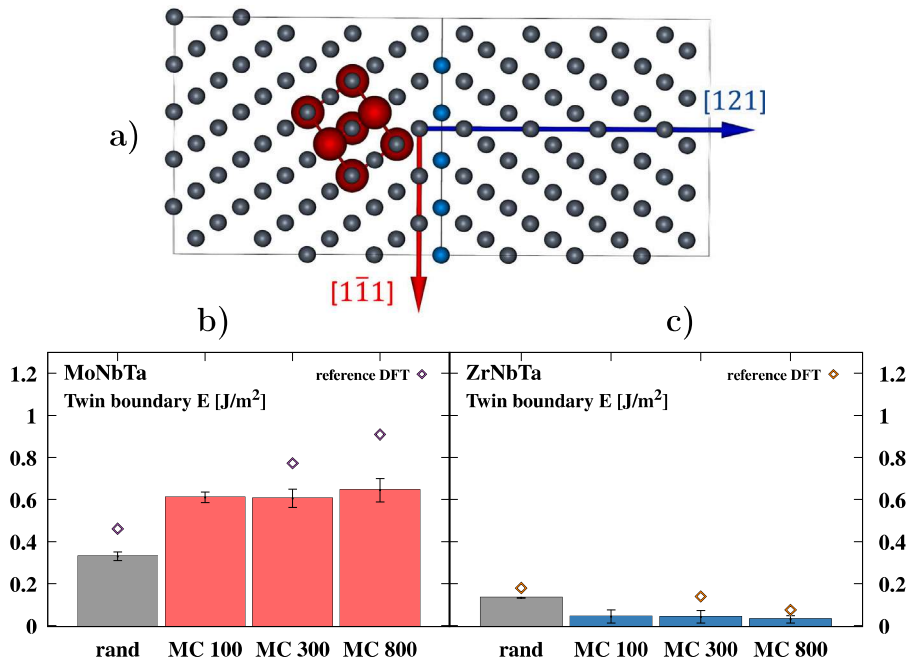


Fig. 7. (a) Structure used to model twin boundary energy with red circles depicting BCC unit cell and blue atoms showing the boundary atoms. Twin boundary energy for random and structures different SRO for (b) MoNbTa and (c) ZrNbTa.

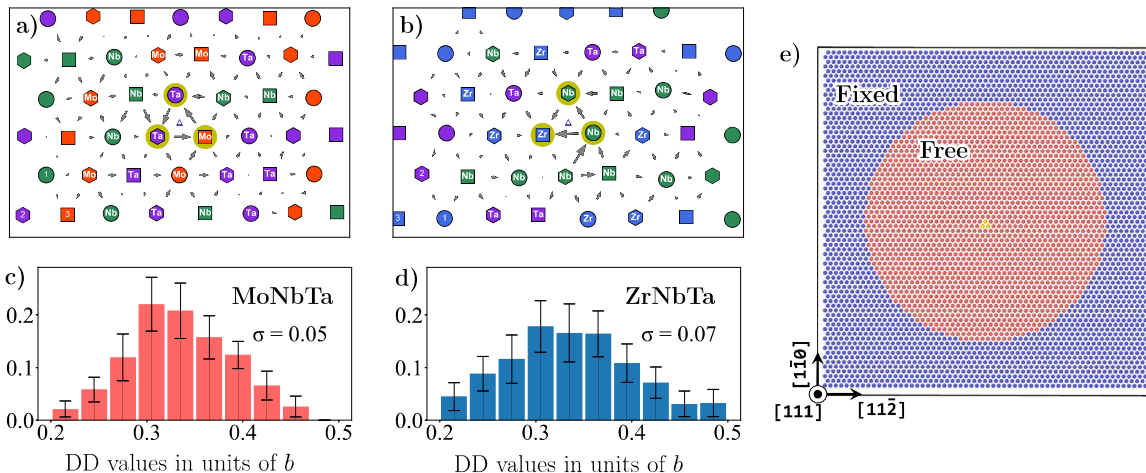


Fig. 8. Differential displacement map for screw dislocation core in (a) MoNbTa and (b) ZrNbTa. Orange, green, purple, and blue colors represent Mo, Nb, Ta, and Zr atomic types respectively. Circular, hexagonal and square-shaped symbols correspond to the first (deepest), second and third (topmost) layers in [111] direction at the span of one Burgers vector. A small hollow triangle shows the geometrical center of the screw dislocation at the stage of its generation. Three atoms marked with dirty-green halo are used for calculations of dd values distribution in (c) MoNbTa and (d) ZrNbTa. (e) Top view of the structure, which holds the dislocation. The circular region in the center marked red represents atoms free for optimization, while the outer region (blue circles) is fixed.

Appendix A. Supplementary data

Supplementary material related to this article can be found online at <https://doi.org/10.1016/j.commatsci.2023.112010>.

References

- [1] M.C. Gao, J.-W. Yeh, P.K. Liaw, Y. Zhang, *High-Entropy Alloys : Fundamentals and Applications*, Springer International Publishing Switzerland, 2016.
- [2] P. Shi, W. Ren, T. Zheng, Z. Ren, X. Hou, J. Peng, P. Hu, Y. Gao, Y. Zhong, P.K. Liaw, Enhanced strength-ductility synergy in ultrafine-grained eutectic high-entropy alloys by inheriting microstructural lamellae, *Nature Commun.* 10 (1) (2019) 489, <http://dx.doi.org/10.1038/s41467-019-10846-2>.
- [3] J.-W. Yeh, S.-K. Chen, S.-J. Lin, J.-Y. Gan, T.-S. Chin, T.-T. Shun, C.-H. Tsau, S.-Y. Chang, Nanostructured high-entropy alloys with multiple principal elements: Novel alloy design concepts and outcomes, *Adv. Eng. Mater.* 6 (5) (2004) 299–303, <http://dx.doi.org/10.1002/adem.200300567>.
- [4] B. Cantor, I. Chang, P. Knight, A. Vincent, Microstructural development in equiatomic multicomponent alloys, *Mater. Sci. Eng. A* 375–377 (2004) 213–218, <http://dx.doi.org/10.1016/j.msea.2003.10.257>.
- [5] S. Ranganathan, Alloyed pleasures: Multimetallic cocktails, *Curr. Sci. India* 85 (2003) 1404–1406, <https://www.scinapse.io/papers/41078916#cited>.
- [6] B. Gludovatz, A. Hohenwarter, K.V.S. Thurston, H. Bei, Z. Wu, E.P. George, R.O. Ritchie, Exceptional damage-tolerance of a medium-entropy alloy CrCoNi at cryogenic temperatures, *Nature Commun.* 7 (1) (2016) 10602, <http://dx.doi.org/10.1038/ncomms10602>.
- [7] T. Tsuru, I. Lobzenko, D. Wei, Synergetic effect of si addition on mechanical properties in face-centered-cubic high entropy alloys: a first-principles study, *Model. Simul. Mater. Sci.* 30 (2) (2022) 024003, <http://dx.doi.org/10.1088/1361-651x/ac455a>.
- [8] D. Wei, L. Wang, Y. Zhang, W. Gong, T. Tsuru, I. Lobzenko, J. Jiang, S. Harjo, T. Kawasaki, Bae, J. Wung, W. Lu, Z. Lu, Y. Hayasaka, T. Kiguchi, N.L. Okamoto, T. Ichitsubo, Kim, H. Seop, T. Furuhara, E. Ma, H. Kato, Metalloid substitution elevates simultaneously the strength and ductility of face-centered-cubic

- high-entropy alloys, *Acta Mater.* 225 (2022) 117571, <http://dx.doi.org/10.1016/j.actamat.2021.117571>.
- [9] O. Senkov, G. Wilks, J. Scott, D. Miracle, Mechanical properties of Nb₂₅Mo₂₅Ta₂₅W₂₅ and V₂₀Nb₂₀Mo₂₀Ta₂₀W₂₀ refractory high entropy alloys, *Intermetallics* 19 (5) (2011) 698–706, <http://dx.doi.org/10.1016/j.intermet.2011.01.004>.
- [10] X. Feng, J. Zhang, Z. Xia, W. Fu, K. Wu, G. Liu, J. Sun, Stable nanocrystalline NbMoTaW high entropy alloy thin films with excellent mechanical and electrical properties, *Mater. Lett.* 210 (2018) 84–87, <http://dx.doi.org/10.1016/j.matlet.2017.08.129>.
- [11] C. Varvenne, A. Luque, W.A. Curtin, Theory of strengthening in fcc high entropy alloys, *Acta Mater.* 118 (2016) 164–176, <http://dx.doi.org/10.1016/j.actamat.2016.07.040>.
- [12] F. Maresca, W.A. Curtin, Theory of screw dislocation strengthening in random BCC alloys from dilute to “high-entropy” alloys, *Acta Mater.* 182 (2020) 144–162, <http://dx.doi.org/10.1016/j.actamat.2019.10.007>.
- [13] S. Rao, B. Akdim, E. Antillon, C. Woodward, T. Parthasarathy, O. Senkov, Modeling solution hardening in BCC refractory complex concentrated alloys: NbTiZr, Nb_{1.5}TiZr_{0.5} and Nb_{0.5}TiZr_{1.5}, *Acta Mater.* 168 (2019) 222–236, <http://dx.doi.org/10.1016/j.actamat.2019.02.013>.
- [14] F. Maresca, W.A. Curtin, Mechanistic origin of high strength in refractory BCC high entropy alloys up to 1900K, *Acta Mater.* 182 (2020) 235–249, <http://dx.doi.org/10.1016/j.actamat.2019.10.015>.
- [15] E. Mak, B. Yin, W. Curtin, A ductility criterion for bcc high entropy alloys, *J. Mech. Phys. Solids* 152 (2021) 104389, <http://dx.doi.org/10.1016/j.jmps.2021.104389>.
- [16] Y. Wang, M. Yan, Q. Zhu, W.Y. Wang, Y. Wu, X. Hui, R. Otis, S.-L. Shang, Z.-K. Liu, L.-Q. Chen, Computation of entropies and phase equilibria in refractory VNbMoTaW high-entropy alloys, *Acta Mater.* 143 (2018) 88–101, <http://dx.doi.org/10.1016/j.actamat.2017.10.017>.
- [17] X. Zhou, H. Wadley, R. Johnson, D. Larson, N. Tabat, A. Cerezo, A. PetfordLong, G. Smith, P. Clifton, R. Martens, T. Kelly, Atomic scale structure of sputtered metal multilayers, *Acta Mater.* 49 (19) (2001) 4005–4015, [http://dx.doi.org/10.1016/S1359-6454\(01\)00287-7](http://dx.doi.org/10.1016/S1359-6454(01)00287-7).
- [18] D.-Y. Lin, S.S. Wang, D.L. Peng, M. Li, X.D. Hui, An *n*-body potential for a Zr–Nb system based on the embedded-atom method, *J. Phys.-Condens. Matter* 25 (10) (2013) 105404, <http://dx.doi.org/10.1088/0953-8984/25/10/105404>.
- [19] L. Ventelon, F. Willaime, E. Clouet, D. Rodney, Ab initio investigation of the peierls potential of screw dislocations in bcc Fe and W, *Acta Mater.* 61 (11) (2013) 3973–3985, <http://dx.doi.org/10.1016/j.actamat.2013.03.012>.
- [20] J. Behler, M. Parrinello, Generalized neural-network representation of high-dimensional potential-energy surfaces, *Phys. Rev. Lett.* 98 (2007) 146401, <http://dx.doi.org/10.1103/PhysRevLett.98.146401>.
- [21] A.P. Bartók, R. Kondor, G. Csányi, On representing chemical environments, *Phys. Rev. B* 87 (2013) 184115, <http://dx.doi.org/10.1103/PhysRevB.87.184115>.
- [22] Y. Shiihara, R. Kanazawa, D. Matsunaka, I. Lobzenko, T. Tsuru, M. Kohyama, H. Mori, Artificial neural network molecular mechanics of iron grain boundaries, *Scr. Mater.* 207 (2022) 114268, <http://dx.doi.org/10.1016/j.scriptamat.2021.114268>.
- [23] O. Senkov, J. Scott, S. Senkova, D. Miracle, C. Woodward, Microstructure and room temperature properties of a high-entropy TaNbHfZrTi alloy, *J. Alloys Compd.* 509 (20) (2011) 6043–6048, <http://dx.doi.org/10.1016/j.jallcom.2011.02.171>.
- [24] J.-P. Couzinié, L. Lilenstein, Y. Champion, G. Dirras, L. Perrière, I. Guillot, On the room temperature deformation mechanisms of a TiZrHfNbTa refractory high-entropy alloy, *Mater. Sci. Eng. A* 645 (2015) 255–263, <http://dx.doi.org/10.1016/j.msea.2015.08.024>.
- [25] T. Kostuchenko, F. Körmann, J. Neugebauer, A. Shapeev, Impact of lattice relaxations on phase transitions in a high-entropy alloy studied by machine-learning potentials, *Npj Comput. Mater.* 5 (1) (2019) 55, <http://dx.doi.org/10.1038/s41524-019-0195-y>.
- [26] X.-G. Li, C. Chen, H. Zheng, Y. Zuo, S.P. Ong, Complex strengthening mechanisms in the NbMoTaW multi-principal element alloy, *Npj Comput. Mater.* 6 (1) (2020) 70, <http://dx.doi.org/10.1038/s41524-020-0339-0>.
- [27] The VASP web-site, <https://www.vasp.at>.
- [28] G. Kresse, J. Furthmüller, Efficient iterative schemes for ab initio total-energy calculations using a plane-wave basis set, *Phys. Rev. B* 54 (1996) 11169–11186, <http://dx.doi.org/10.1103/PhysRevB.54.11169>.
- [29] G. Kresse, J. Furthmüller, Efficiency of ab-initio total energy calculations for metals and semiconductors using a plane-wave basis set, *Comput. Mater. Sci.* 6 (1) (1996) 15–50, [http://dx.doi.org/10.1016/0927-0256\(96\)00008-0](http://dx.doi.org/10.1016/0927-0256(96)00008-0).
- [30] J.P. Perdew, K. Burke, M. Ernzerhof, Generalized gradient approximation made simple, *Phys. Rev. Lett.* 77 (1996) 3865–3868, <http://dx.doi.org/10.1103/PhysRevLett.77.3865>.
- [31] A.P. Bartók, M.C. Payne, R. Kondor, G. Csányi, Gaussian approximation potentials: The accuracy of quantum mechanics, without the electrons, *Phys. Rev. Lett.* 104 (2010) 136403, <http://dx.doi.org/10.1103/PhysRevLett.104.136403>.
- [32] P. Rowe, G. Csányi, D. Alfè, A. Michaelides, Development of a machine learning potential for graphene, *Phys. Rev. B* 97 (2018) 054303, <http://dx.doi.org/10.1103/PhysRevB.97.054303>.
- [33] J. Behler, First principles neural network potentials for reactive simulations of large molecular and condensed systems, *Angew. Chem. Int. Edn* 56 (42) (2017) 12828–12840, <http://dx.doi.org/10.1002/anie.201703114>.
- [34] A. Thompson, L. Swiler, C. Trott, S. Foiles, G. Tucker, Spectral neighbor analysis method for automated generation of quantum-accurate interatomic potentials, *J. Comput. Phys.* 285 (2015) 316–330, <http://dx.doi.org/10.1016/j.jcp.2014.12.018>.
- [35] N. Artrith, A. Urban, G. Ceder, Efficient and accurate machine-learning interpolation of atomic energies in compositions with many species, *Phys. Rev. B* 96 (2017) 014112, <http://dx.doi.org/10.1103/PhysRevB.96.014112>.
- [36] The aenet web-site, <http://ann.atomistic.net/>.
- [37] A.M. Cooper, J. Kästner, A. Urban, N. Artrith, Efficient training of ANN potentials by including atomic forces via taylor expansion and application to water and a transition-metal oxide, *Npj Comput. Mater.* 6 (1) (2020) 54, <http://dx.doi.org/10.1038/s41524-020-0323-8>.
- [38] A. Singraber, J. Behler, C. Dellago, Library-based LAMMPS implementation of high-dimensional neural network potentials, *J. Chem. Theory Comput.* 15 (3) (2019) 1827–1840, <http://dx.doi.org/10.1021/acs.jctc.8b00770>.
- [39] J. Behler, Atom-centered symmetry functions for constructing high-dimensional neural network potentials, *J. Chem. Phys.* 134 (7) (2011) 074106, <http://dx.doi.org/10.1063/1.3553717>.
- [40] P.-A. Geslin, D. Rodney, Microelasticity model of random alloys. Part I: mean square displacements and stresses, *J. Mech. Phys. Solids* 153 (2021) 104479, <http://dx.doi.org/10.1016/j.jmps.2021.104479>.
- [41] N.L. Okamoto, K. Yuge, K. Tanaka, H. Inui, E.P. George, Atomic displacement in the CrMnFeCoNi high-entropy alloy – scaling factor to predict solid solution strengthening, *AIP Adv.* 6 (12) (2016) 125008, <http://dx.doi.org/10.1063/1.4971371>.
- [42] S. Plimpton, Fast parallel algorithms for short-range molecular dynamics, *J. Comput. Phys.* 117 (1) (1995) 1–19, <http://dx.doi.org/10.1006/jcph.1995.1039>.
- [43] LAMMPSWeb Page, Available online: <https://lammps.sandia.gov>.
- [44] HidekiMori-CIT, Aenet-Lammps, Available online: <https://github.com/HidekiMori-CIT/aeenet-lammps>.
- [45] H. Mori, T. Ozaki, Neural network atomic potential to investigate the dislocation dynamics in bcc iron, *Phys. Rev. Mater.* 4 (2020) 040601, <http://dx.doi.org/10.1103/PhysRevMaterials.4.040601>.
- [46] A. Van De Walle, P. Tiwary, M. De Jong, D. Olmsted, M. Asta, A. Dick, D. Shin, Y. Wang, L. Chen, Z. Liu, Efficient stochastic generation of special quasirandom structures, *Calphad: Comput. Coupling Phase Diagr. Thermochem.* 42 (2013) 13–18, <http://dx.doi.org/10.1016/j.calphad.2013.06.006>.
- [47] X. Kong, C. Hu, Z. Duan, *Principal Component Analysis Networks and Algorithms*, Science Press, Beijing and Springer Nature, Singapore, 2017.
- [48] J. Ding, Q. Yu, M. Asta, R.O. Ritchie, Tunable stacking fault energies by tailoring local chemical order in CrCoNi medium-entropy alloys, *Proc. Natl Acad. Sci.* 115 (36) (2018) 8919–8924, <http://dx.doi.org/10.1073/pnas.1808660115>.
- [49] H. Ikehata, N. Nagasako, T. Furuta, A. Fukumoto, K. Miwa, T. Saito, First-principles calculations for development of low elastic modulus Ti alloys, *Phys. Rev. B* 70 (2004) 174113, <http://dx.doi.org/10.1103/PhysRevB.70.174113>.
- [50] J.P. Hirth, J. Lothe, *Theory of Dislocations*, second ed., Wiley, New York, 1982.
- [51] V. Vítek, R.C. Perrin, D.K. Bowen, The core structure of 1/2(111) screw dislocations in b.c.c. crystals, *Philos. Mag.: J. Theoret. Exp. Appl. Phys.* 21 (1973) 1049–1073, <http://dx.doi.org/10.1080/14786437008238490>.
- [52] S. Yin, J. Ding, M. Asta, R.O. Ritchie, Ab initio modeling of the energy landscape for screw dislocations in body-centered cubic high-entropy alloys, *Npj Comput. Mater.* 6 (1) (2020) 110, <http://dx.doi.org/10.1038/s41524-020-00377-5>.
- [53] S.L. Frederiksen, K.W. Jacobsen, Density functional theory studies of screw dislocation core structures in bcc metals, *Phil. Mag.* 83 (3) (2003) 365–375, <http://dx.doi.org/10.1080/0141861021000034568>.
- [54] S. Yin, Y. Zuo, A. Abu-Odeh, H. Zheng, X.-G. Li, J. Ding, S.P. Ong, M. Asta, R.O. Ritchie, Atomistic simulations of dislocation mobility in refractory high-entropy alloys and the effect of chemical short-range order, *Nature Commun.* 12 (1) (2021) 4873, <http://dx.doi.org/10.1038/s41467-021-25134-0>.
- [55] L. Dezerald, D. Rodney, E. Clouet, L. Ventelon, F. Willaime, Plastic anisotropy and dislocation trajectory in BCC metals, *Nature Commun.* 7 (1) (2016) 11695, <http://dx.doi.org/10.1038/ncomms11695>.
- [56] D.C. Chrzan, M.P. Sherburne, Y. Hanlumyuang, T. Li, J.W. Morris, Spreading of dislocation cores in elastically anisotropic body-centered-cubic materials: The case of gum metal, *Phys. Rev. B* 82 (2010) 184202, <http://dx.doi.org/10.1103/PhysRevB.82.184202>.